Chemistry-Mediated Ostwald Ripening in Carbon-Rich C/O Systems at Extreme Conditions

Rebecca K. Lindsey,[*,†] Nir Goldman,[†,‡] Laurence E. Fried,[†] and Sorin Bastea[*,†]

†*Physical and Life Sciences Directorate, Lawrence Livermore National Laboratory, Livermore, California 94550, United States*

‡*Department of Chemical Engineering, University of California, Davis, California 95616, United States*

E-mail: lindsey11@llnl.gov; bastea2@llnl.gov

Phone: +1-925-422-0915; +1-925-422-2178

Abstract

There is significant interest in establishing a capability for tailored synthesis of next-generation carbon-based nanomaterials due to their broad range of applications and high degree of tunability. High pressure (e.g. shockwave-driven) synthesis holds promise as an effective discovery method, but experimental challenges preclude elucidating the processes governing nanocarbon production from carbon-rich precursors that could otherwise guide efforts through the prohibitively expansive design space. Here we report findings from large scale atomistically-resolved simulations of carbon condensation from C/O mixtures subjected to extreme pressures and temperatures, made possible by machine-learned reactive interatomic potentials. We find that liquid nanocarbon formation follows classical growth kinetics driven by Ostwald ripening (i.e. growth of large clusters at the expense of shrinking small ones) and obeys dynamical scaling in a process mediated by carbon chemistry in the surrounding reactive fluid. The results provide direct insight into carbon condensation in a representative system and pave the way for its exploration in higher complexity organic materials. They also suggest that simulations using machine-learned interatomic potentials could eventually be employed as *in-silico* design tools for new nanomaterials.

1 Introduction

Carbon exhibits a remarkable propensity for forming nanomaterials with unusual physical and chemical properties arising from its ability to engage in different covalent bonding states.[1–4] Many of these "next-generation" nanomaterials, which include nanodiamonds, nanographite, amorphous nanocarbon, nano-onions etc., are currently being studied for possible applications spanning quantum computing to bio-imaging,[1] and ongoing research suggests that high-pressure synthesis could lead to the discovery and possibly the tailored design of many more. Both laser-driven shock[5,6] and detonation experiments[3,7,8] can be used to drive carbon-rich materials to the 1000s of K and 10s of GPa conditions under which complex processes lead to the formation of 2-10 nm nanocarbons within 100s of nanoseconds. However, the precise chemical and physical phenomena governing nanocarbon formation under elevated pressure and temperature largely remain *terra incognita*, due in part to the formidable challenges associated with studying systems at such extreme states. Recent experiments on nanodiamond production from hydrocarbons subjected to conditions similar with those of planetary interiors[5] offer some clues on possible carbon condensation mechanisms, but the landscape of systems and conditions under which intense compression could yield interesting nanomaterials is too vast to be explored using experiments alone.

Atomistic simulations can be leveraged to provide insight into the fundamental processes controlling formation of nanocarbon materials, and could also serve as a design tool to help guide experimental efforts. However, the associated temporal and spatial scales are inaccessible to highly-predictive first-principles based approaches, e.g. Kohn-Sham Density Functional Theory (DFT), while molecular mechanics models applicable to materials exposed to extreme temperatures and pressures are quite scarce. Recently, we proposed a new machine-learned interatomic model and modeling paradigm, the Chebyshev Interaction Model for Efficient Simulations (ChIMES),[9–15] which is capable of retaining "quantum accuracy" while maintaining the computational efficiency of a molecular mechanics approach.

In this paper we significantly advance the modeling effort initiated in ref. 6 by performing an in-depth investigation of carbon condensation (precipitation) in oxygen deficient C/O mixtures at high pressures and temperatures. To this end, we leveraged the ChIMES framework to both substantially extend the simulations of Ref. [6] and perform new simulations at different C/O ratios. C/O systems are often employed in practical applications and are excellent candidates for uncovering the essential features of this complex process due to their relative simplicity. For example, carbon monoxide (CO) has been used for carbon nanotube production under ambient to slightly elevated pressures, and explored as a precursor for other nanocarbon materials,[16–18] while shock compression of liquid CO to 10s of GPa has yielded convincing evidence of nanocarbon formation.[6,19] Furthermore, C/O systems serve as a logical stepping stone to the CNO (and CHNO) organic compounds traditionally employed for high-pressure nanodiamond synthesis (e.g. benzotrifuroxan, $C_6N_6O_6$),[8] or those recently shown to yield carbon nano-onions (e.g. bis(nitrofurazano)furazan, $C_6N_8O_8$).[7]

Carbon condensation in organic systems subject to high temperatures and pressures is clearly a non-equilibrium process akin to phase separation in mixtures quenched from a homogenous phase into a two-phase region,[20,21] yet this connection has only been partially explored;[22–24] notably, phase separation concepts remain very relevant for nanoparticle synthesis.[25] Chemical bonding adds a new dimension to the classical problem of segregation kinetics and can generate interesting and consequential features, e.g., by introducing length scales that determine system morphology.[26] Atomistic modeling could help elucidate such problems but the research remains in its infancy, with applications to carbon precipitation nearly nonexistent. Herein we leverage the machine-learned ChIMES reactive interatomic potential framework to simulate carbon-rich C/O mixtures and address open

questions surrounding formation of nanocarbon from highly compressed organic materials, e.g.:

- What is the role of chemistry during carbon condensation?

- How do carbon clusters evolve, both structurally and chemically, and what is their growth mechanism?

- How does overall system composition influence carbon cluster formation?

Our results provide an atomistically-resolved view of carbon clustering in a condensed phase reactive system and make possible for the first time a comprehensive analysis of this process, thereby opening new investigative avenues that could lead to *in-silico* design of next-generation nanomaterials.

2   Methods

Unless otherwise stated, simulations were performed in the NVT ensemble at 6500 K and 2.5 g/cm^3. These conditions approximately correspond to the Hugoniot state point achieved by a 7 km/s shock into cryogenic liquid CO, thereby mimicking the classic experiments of Nellis and coworkers[19] that first suggested carbon precipitation from a shocked organic liquid. Simulations were initialized as a fluid of randomly packed CO and CO_2 molecules at a ratio yielding the target C/O composition, and allowed to relax for 10 ps at $\simeq$ 100 K to reduce unfavorable close contact due to packing; velocities were then rescaled yielding a system temperature of 6500 K. We note that system initialization protocols have a negligible influence on simulation predictions for this work due to the rapid dynamics occurring under such elevated temperatures. For example, results from exploratory simulations initialized as a system of randomly packed C and O atoms and those from exploratory simulations initialized from equilibrated DFT-MD simulations at 6500 K and 2.5 g/cm^3 were statistically indistinguishable. All simulations were run using the LAMMPS[27] software suite, and interatomic interactions were evaluated using the ChIMES interatomic potential.[12] These models, which are machine-learned to Kohn–Sham density functional theory[28] (DFT), are capable of yielding "quantum accurate" predictions for structure, dynamics, and speciation, provide several-orders-of-magnitude increases in efficiency over first principles methods, and exhibit computational efficiency that scales linearly with system size. A detailed description and validation of the ChIMES model for this system is available in ref. 12. We note that the ChIMES model utilized herein, a library for computing ChIMES interactions, and source code necessary for its use within LAMMPS is available in ref. 29.

In this work, carbon condensates are defined as any set of carbon atoms containing at least 10 members, instantaneously separated by no more than $r_{CC} = 1.9$ Å from their nearest neighbor within a candidate cluster (with r_{CC} corresponding to the location of the first minimum of the C—C radial pair distribution function, RDF). For clusters containing both atom types, oxygen atoms within $r_{CO} = 1.8$ Å of a cluster carbon were also counted, with r_{CO} taken as the location of the first minimum of the corresponding RDF. While the choice of clustering criteria may have some effect on predictions, e.g. on cluster radii, we note that our overall analysis and conclusions remain unchanged.

3   Results

Carbon condensation predictions from atomistic simulations are vulnerable to finite size effects,[12,30] since precipitation progresses through formation and evolution of a well-defined nano-sized carbon cluster population. As shown in Figure 1, simulations for 5 systems sizes spanning 4 orders of magnitude (i.e. $\approx 1.25 \times 10^2$ to 1.25×10^6 atoms) were investigated to quantify the extent of such effects. We summarize salient findings here, noting that further discussion is available in the Supporting Information. All systems containing more than $\approx 1.25 \times 10^2$ atoms yielded at least one cluster, though clusters did
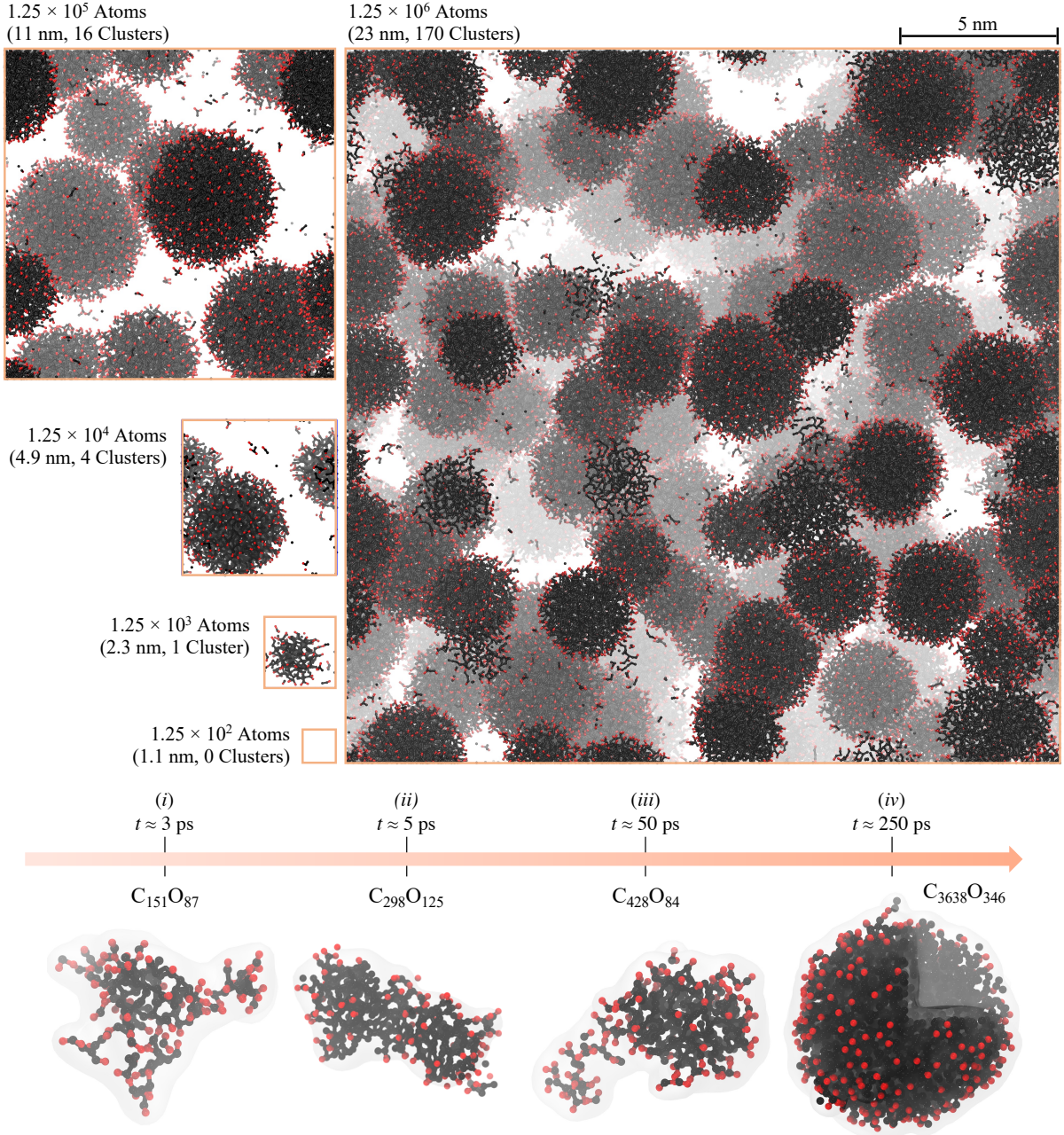
Figure 1: Top: snapshots for systems containing $\approx 1.25 \times 10^2$, 1.25×10^3, 1.25×10^4, 1.25×10^5, and 1.25×10^6 atoms at 0.25 ns. Images are to scale, and for clarity, only show atoms participating in cluster formation. Bottom: representative cluster growth timeline; a similar figure is included in ref. 6.

not become morphologically and compositionally similar until system sizes reached at least 1.25×10^4 atoms. This is notable within the context of recent studies of this system; ultra-fast laser-driven shock experiments, which probe a target system on similar scales (i.e. 1 μm and 10s to 100s of ps) have confirmed growth of nano-sized carbon condensates within 50 ps.[6] Conversely,

recent DFT-MD simulations found only small covalent species of $C_{2n}O_n$ stoichiometry,[30] with $n \approx 21$. The discrepancy between the DFT-MD result and those from the present simulations (and available experiments) ultimately stems from the high computational expense associated with DFT, which limits system scales to $\mathcal{O}\,100$ atoms and 10s of ps. Increasing system size in the current simulations has the primary effect of increasing the range of observed cluster dimensions. As expected, late time cluster growth is significantly impacted by system size; nevertheless, the average cluster radii and qualitative behavior are consistent across all systems with $\geq 1.25 \times 10^4$ atoms.

To determine how system composition impacts condensate formation, systems with eight C:O ratios were investigated in addition to the 1:1 C:O system described above. The initial compositions of these systems ranged from 95/5, to 25/75% CO/CO_2 and, as discussed in the Supporting Information, carbon clusters were found to form within 25 ps in each of them. We focus here on the 100% CO and 80/20% CO/CO_2 systems, which we henceforth distinguish by their respective C:O ratios, i.e. 1:1 and 5:6. We note that, in contrast to the 1:1 case, cluster morphology, composition, and formation kinetics for the 5:6 C:O system were largely unaffected by system size, provided $\geq 1.25 \times 10^4$ atoms were used. For the remainder of this work, simulation results for the 1:1 system will correspond to a single 500 ps simulation of 1.25×10^6 atoms, whereas results for the 5:6 system are an average over 4 independent 250 ps simulations of 1.25×10^5 atoms; when results are being compared between the 1:1 and 5:6 cases, data for both concentrations correspond to the latter simulation protocol, unless otherwise stated. We note that 5:6 C:O simulations were run at 6500 K and 2.46 g/cm^3, yielding the same initial pressure as the 1:1 C:O simulation at 6500 K and 2.5 g/cm^3.

3.1 Cluster Evolution

Figure 1 provides snapshots of representative carbon clusters during a typical growth progression, suggesting a few notable features of their evolution. At early time (Figure 1.i), small extended polymeric fragments are observed, typically showing $C_{2n}O_n$ stoichiometry, consistent with previous, small-scale DFT studies.[30] As time passes (Figures 1.ii and 1.iii), the clusters become more compact, begin to densify and expel interior oxygen, leading to the formation of large spherical liquid carbon droplets, with oxygen atoms located primarily on their surface (Figure 1.iv). Final snapshots for cluster-containing systems (i.e Figure 1), suggest that smaller clusters are morphologically distinct from their larger counterparts, and increasing system size leads to a broader cluster size distribution.

A quantitative picture of cluster evolution is provided in Figure 2, which shows reduced average radial density profiles, $\rho(r/R_g)$, for the 1:1 system cluster population, along with time resolved average cluster radii of gyration R_g (i.e. the average distance between cluster carbon atoms and cluster carbon center of mass). Note that plotted radii and density profiles correspond to hyperbolic tangent fits to each histogrammed $\rho(r/R_g)$ of the form: $\rho = 0.5\rho_0 \left\{ 1 - \tanh\left[w_0^{-1}\left(r/R_g - d_0\right)\right]\right\}$, with $w_0 = w/R_g$ and $d_0 = d/R_g$, where ρ_0 is the density in the center of the cluster, w is the interfacial width, and d is the distance from the cluster centroid to the interface. (We note that the interface location - d - is a suitable measure for the cluster size, but it is numerically more difficult to determine precisely for individual clusters than R_g, which we employ below).

For clarity, the present analysis considers only carbon atoms within a cluster; since oxygen is located almost exclusively at the exterior in mature clusters, this choice has minimal influence on late time results. These profiles indicate a transition from extended, low-density clusters at early time to clusters with an interior density of approximately 3 g/cm^3. At the same time, the cluster interface steepens considerably, with the interfacial width, w, decreasing from approximately 2.50 to a stable value of $\simeq 1.25$ Å over 50 ps. Early time density profile curves correspond to clusters
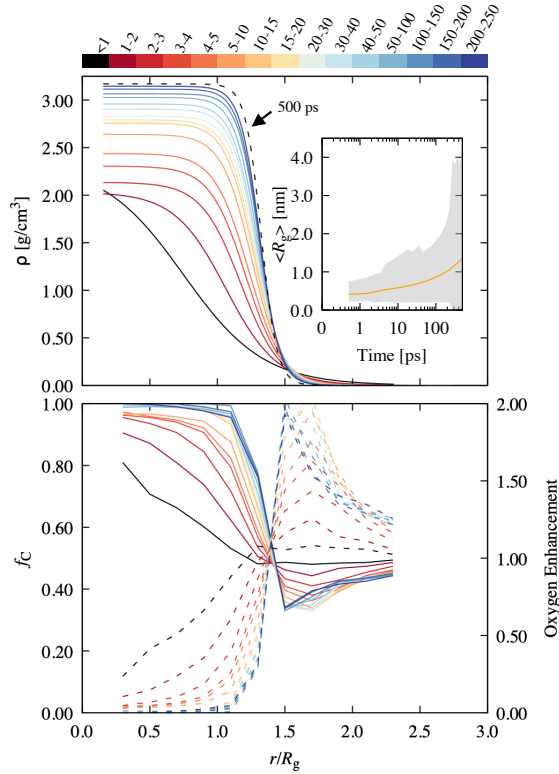
Figure 2: Top: Reduced radial density profiles, $\rho(r/R_g)$, and time-resolved average radius of gyration (inset), $\langle R_g \rangle$, for the 1:1 C:O system. Plotted radii and density profiles correspond to hyperbolic tangent fits to each histogrammed $\rho(r/R_g)$. The black dashed curve gives the profile at 500 ps and the shaded region in the $\langle R_g \rangle$ inset figures gives the maximum and minimum observed R_g at each time block, while the orange line gives the average value. Bottom: Radial atomic fraction of carbon (f_C, solid lines) and oxygen enrichment (f_O/f_C, dashed lines) emanating from cluster centroids. The color bars provide the corresponding time range for each line, in ps, unless otherwise specified.

such as those in Figures 1.i, which exhibit approximately $C_{2n}O_n$ stoichiometry and appear to be of covalent nature (note that our models do not explicitly treat bonding as is common in molecular mechanics formalisms), whereas late clusters (Figures 1.iv) are best described as liquid carbon droplets. As shown in Fig. 2 (inset) the average cluster radius R_g increases

with time, with the largest clusters reaching sizes of a few nanometers. Additional radial density profiles and average radii of gyration for different C:O ratios are available in the Supporting Information. In general, we find that cluster structural evolution is mostly uncoupled from system composition.

Cluster chemical composition evolution is a crucial aspect of the carbon precipitation and growth kinetics. Time resolved, radial atomic fractions emanating from cluster centroids are given in Figure 2. Note that these curves are obtained by considering all atoms in the system within r/R_g of a given cluster centroid. We find that at early times cluster interiors (i.e $r/R_g < 1$) have a sizable oxygen content, with values as large as 20%. As time progresses, oxygen migrates to the exterior, resulting in essentially pure liquid carbon droplets, surrounded by carbon depletion and oxygen enrichment layers (see Figure 2) with approximate CO_2 stoichiometry. The amount of oxygen within the growing clusters appears to decay exponentially in time, with a relaxation time constant of $\simeq$ 5 ps (see Supporting Information). A similar analysis of the 5:6 C:O system (see Supporting Information) shows that the overall C:O ratio has little qualitative effect on the cluster evolution, indicating that under these conditions the densification and oxygen elimination processes are not very sensitive to system stoichiometry. As the average cluster composition stabilizes, so does the makeup of the reactive fluid that the clusters are immersed in; time-resolved molecular speciation, shows that this is chiefly comprised of CO_2, CO, and free oxygen atoms at late times (see Supporting Information).

The total cluster volume fraction, $\langle f_{v,clu} \rangle$, calculated from individual cluster radii of gyration, exhibits behavior characteristic of precipitation from a supersaturated solution, with an initial delay followed by step-like growth and rapid leveling off to a value dependent on the system composition. The delay is slightly longer in the 5:6 system relative to the 1:1 case, likely due to the lower initial carbon "supersaturation",

6

while the final condensed carbon volume fraction is smaller. It is worth noting that the observed "supersaturation" dependence of the delay is consistent with classical nucleation effects in mixtures,[31] which determine the persistence of an initial metastable, single fluid phase in a two-phase region.

As already noted in ref. 6, the volume fraction for the 1:1 system at $\simeq$ 50 ps ($\simeq$ 8 %) agrees with experimental results for CO compressed on time scales of 100s of ps to thermodynamic conditions similar to these simulations, and with chemical equilibrium calculations that predict the end state of the system .[6] Figure 3 indicates that the transition to near constant total cluster volume fraction coincides with a maximum in the number of clusters present in the system for both systems discussed here (1:1 and 5:6 C:O ratios), suggesting that the later time evolution is dominated by coarsening kinetics.
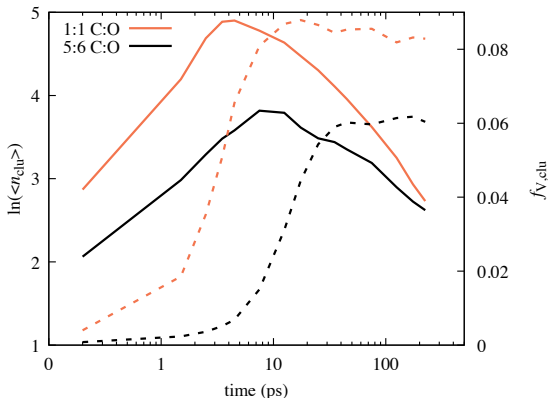

Figure 3: Natural log of the average number of clusters, $\ln\left(\langle n_{\mathrm{clu}}\rangle\right)$, and average cluster volume fraction, $\langle f_{\mathrm{v,clu}}\rangle$ in the 1:1 and 5:6 CO systems.

3.2 Growth kinetics

We quantify cluster growth kinetics through analysis of the average cluster radius $\langle R_{\mathrm{g}}\rangle$ as a function of time. Figure 4(left) shows that at late times both systems (i.e. 1:1 and 5:6 C:O) exhibit linear growth in the average cluster volume, $\langle R_{\mathrm{g}}\rangle^3$ vs t, i.e. $\langle R_{\mathrm{g}}\rangle \propto t^{\frac{1}{3}}$. This behavior is consistent with coarsening via Ostwald ripening

(i.e. evaporation - condensation or dissolution - re-deposition mechanism), described by Lifshitz, Slyozov and Wagner (LSW),[32–34] in which diffusional mass transfer occurs between the clusters, with clusters smaller than the average size shrinking and the larger ones growing. The present results thus establish the relevance of LSW phenomenology for carbon condensation in a high pressure - high temperature chemically reactive environment[1]. Hydrodynamic effects are known to determine fluid phase separations at large, $\approx$ 0.5 volume fractions of the minority phase (here carbon);[35] for intermediate values, direct cluster coagulation (Brownian aggregation) is expected to yield volume fraction-dependent growth,[35,36] which is believed to be dominant in detonation-driven carbon condensation on long ($\mathcal{O}$ 100s ns) time scales.[22,23,37] Such scales are beyond the practical reach of our atomistic simulations. Nevertheless, we note that the LSW mechanism identified here plays a crucial role in cluster coagulation by inducing composition correlations between neighbouring clusters which drive their direct aggregation;[38] a possible example is in ref. 37.

Coarsening in phase separating systems is known to exhibit dynamical scaling, characterized by a time-invariant cluster population when scaled by the average cluster size.[20,21] We find that the carbon cluster size distribution in the current simulations is largely self-similar, and compares well with the original LSW distribution[32] (see Figure 4). Note that differences are likely due to volume fraction effects.[34] This further suggests that cluster growth through atomic diffusive flux is indeed the leading coarsening mechanism. However, we note that in the present system the mass transfer process is more complex than in classical fluid or solid solutions, in which minority phase atoms "evaporate" from smaller clusters, diffuse through the surrounding solvent matrix and "condense" on larger clusters. In particular, the carbon clusters are immersed in a reactive fluid primarily composed of CO_2, CO,

---

[1]An important feature of the LSW mechanism is that the average cluster size is the current critical nucleus size for the system. This interpretation is likely valid for the present case as well; the idea was employed in ref. 24
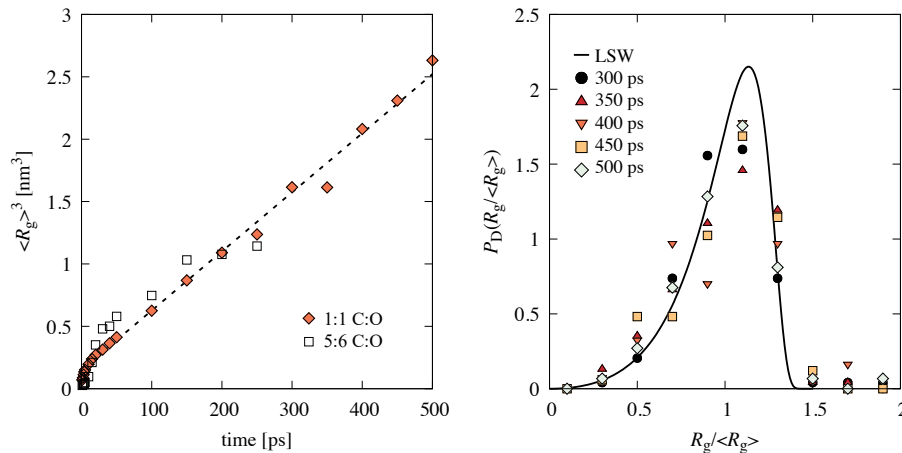
Figure 4: Left: Cubed average radius of gyration, $\langle R_g \rangle^3$, as a function of time, for the 1:1 and 5:6 C:O systems. Right: Cluster size distributions in terms of reduced cluster radii of gyration, $R_g/\langle R_g \rangle$, for $t = 300$ to 500 ps in the 1.25×10^6 atom 1:1 C:O system. The cluster size distribution predicted by LSW theory is given by the solid black line.

and O with virtually no free C atoms. Given the properties of the oxygen-rich cluster surface layer (see Fig. 2) and the make-up of the reactive fluid, carbon transfer between the clusters appears to principally involve the reactions $C_n + CO_2 \leftrightarrow C_{n-1} + 2CO$ and $C_n + O \leftrightarrow C_{n-1} + CO$, proceeding predominantly forward for small clusters and backward for larger ones, with CO and CO_2 being the main carbon carriers between the clusters. We illustrate this atomic-level "hitchhiking" process in Figure 5, which shows the chemical bonding environments of a single carbon atom as it travels from one cluster to another. As can be seen in the figure (and corresponding Supporting Information movie), the carbon atom shuttling between clusters reacts throughout its journey, associating with different oxygen atoms along the way to form CO and CO_2 molecules. This chemical picture likely becomes much more complex for organic systems that also contain nitrogen and/or hydrogen. Subsequent system quenching to lower pressures and temperatures (e.g. occurring in the wake of a shockwave) will have significant impact on the carbon condensation process, both through the phase transformation of the carbon nanodroplets to other carbon nanoallotropes, e.g. nanodiamond, and possible inhibition of chemical reactions between the clusters and the surrounding reactive fluid. These effects will play an important role in determining the properties of clusters that are ultimately recovered from experiments. Simulation studies of this quenching process will be the subject of future investigations.

4 Discussion

We have presented atomistic simulations of chemistry-coupled carbon condensation and an in-depth analysis addressing long standing questions related to high pressure nanocarbon synthesis in organic systems. We find that this process can be suppressed by small system sizes, e.g. hundreds of atoms typically accessible to DFT-based methods, and that much larger simulations are needed to capture its physicochemical features. Our simulations have yielded a comprehensive picture of carbon cluster evolution in carbon-rich C:O systems at extreme conditions, which is surprisingly similar with canonical phase separation in fluid mixtures, but also exhibits unique features typical of reactive systems. At early times extended, polymeric seed clusters of approximate $C_{2n}O_n$ composition form rapidly as excess carbon precipitates out of the "supersaturated" solution. At the next stage, these clusters
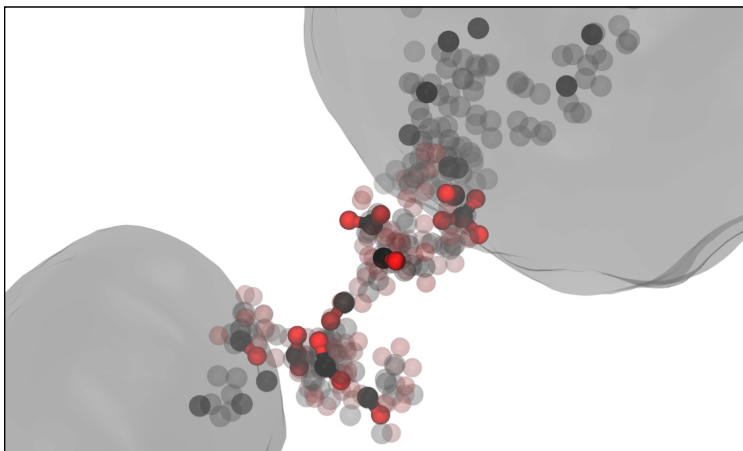
8

Figure 5: Reactive transport trajectory of a single carbon atom (black) from a small (lower left) to a relatively larger cluster (upper right). Large transparent blobs provide the approximate cluster carbon isosurface in a single frame, and oxygen atoms bonded to the carbon atom during transport are colored in red. For visual clarity, only a handful of frames showing the tracked carbon atom (and oxygen atoms bonded to it) have been rendered opaquely. A movie of this process is available in the Supporting Information.

densify by expelling interior oxygen and become spherical, ultimately exhibiting purely molten-carbon interiors and oxygen-decorated exteriors. Clusters occupy $\simeq 8\%$ of system volume in the 1:1 C:O system, and possess interior densities of 3 g/cm^3, typical of liquid carbon.

Their growth on hundreds of picoseconds time-scales occurs mainly through Ostwald ripening and generates cluster populations that obey dynamical scaling. However, in contrast to the classical picture prevailing in simple solid or fluid mixtures, inter-cluster carbon diffusive transport is chemistry-mediated and may perhaps be described as *atomic "hitchhiking" via chemical bonding*. These features are likely to play an important role in predicting and possibly controlling the condensation process and properties of resulting nanocarbon particles. The present simulation approach can be extended to CNO[15] and CHNO systems, and could eventually be leveraged as an *in-silico* material design tool, substantially lowering experimental barriers associated with creating and refining carbon nanoallotrope synthesis protocols.

5   Data Availability

The simulation datasets generated and/or analyzed in the current study are available upon reasonable request.

6   Code Availability

MD simulations were performed using the LAMMPS software package, available at ref. 39. The library used for computing ChIMES interactions and paramaeter set employed in this work are available at ref. 29.

Supporting Information Available

- SI.pdf: Supporting information for this article

- Ripening.gif: Simulation trajectory movie corresponding to Fig 5

References

(1) Georgakilas, V.; Perman, J.; Tucek, J.; Zboril, R. Broad family of carbon nanoallotropes: classification, chemistry, and applications of fullerenes, carbon cots, canotubes, graphene, nanodiamonds, and combined superstructures. *Chemical Reviews* **2015**, *115*, 4744–4822.

(2) Baker, S.; Baker, G. Luminescent carbon nanodots: emergent nanolights. *Angewandte Chemie* **2010**, *49*, 6726–6744.

(3) Mochalin, V. N.; Shenderova, O.; Ho, D.; Gogotsi, Y. The properties and applications of nanodiamonds. *Nature nanotechnology* **2012**, *7*, 11.

(4) Chang, Y.-R.; Lee, H.-Y.; Chen, K.; Chang, C.-C.; Tsai, D.-S.; Fu, C.-C.; Lim, T.-S.; Tzeng, Y.-K.; Fang, C.-Y.; Han, C.-C.; Chang, H.-C.; Fann, W. Mass production and dynamic imaging of fluorescent nanodiamonds. *Nature nanotechnology* **2008**, *3*, 284.

(5) Kraus, D.; Vorberger, J.; Pak, A.; Hartley, N.; Fletcher, L.; Frydrych, S.; Galtier, E.; Gamboa, E.; Gericke, D.; Glenzer, S.; Granados, E.; MacDonald, M.; MacKinnon, A.; McBride, E.; Nam, I.; Neumayer, P.; Roth, M.; Saunders, A.; Schuster, A.; Sun, P.; van Driel, T.; Döppner, T.; Falcone, R. Formation of diamonds in laser-compressed hydrocarbons at planetary interior conditions. *Nature Astronomy* **2017**, *1*, 606–611.

(6) Armstrong, M.; Lindsey, R.; Goldman, N.; Nielsen, M.; Stavrou, E.; Fried, L.; Zaug, J.; Bastea, S. Ultrafast shock synthesis of nanocarbon from a liquid precursor. *Nature Communications* **2020**, *11*, 353.

(7) Bagge-Hansen, M.; Lauderbach, L.; Hodgin, R.; Bastea, S.; Fried, L.; Jones, A.; van Buuren, T.; Hansen, D.; Benterou, J.; May, C.; Graber, T.; B, J.; Ilavsky, J.; T, W. Measurement of carbon condensates using small-angle x-ray scattering during detonation of the high explosive hexanitrostilbene. *Journal of Applied Physics* **2015**, *117*, 245902.

(8) Batsanov, S.; Osavchuk, A.; Naumov, S.; Efimov, A.; Mendis, B.; Apperley, D.; Batsanov, A. Synthesis and properties of hydrogen-free detonation diamond. *Propellants,Explosives,Pyrotechnics* **2015**, *40*, 39–45.

(9) Lindsey, R. K.; Fried, L. E.; Goldman, N. ChIMES: A Force Matched Potential with Explicit Three-Body Interactions for Molten Carbon. *J. Chem. Theory Comput.* **2017**, *13*, 6222–6229.

(10) Goldman, N.; Aradi, B.; Lindsey, R. K.; Fried, L. E. Development of a Multi-center Density Functional Tight Binding Model for Plutonium Surface Hydriding. *Journal of chemical theory and computation* **2018**, *14*, 2652–2660.

(11) Lindsey, R. K.; Fried, L. E.; Goldman, N. Application of the ChIMES Force Field to Non-Reactive Molecular Systems: Water at Ambient Conditions. *Journal of chemical theory and computation* **2019**, *15*, 436–447.

(12) Lindsey, R. K.; Goldman, N.; Fried, L. E.; Bastea, S. Development of the ChIMES Force Field for Reactive Molecular Systems: Carbon Monoxide at ExtremeConditions. *Journal of Chemical Physics* **2020**, *153*, 054103.

(13) Lindsey, R. K.; Fried, L. E.; Goldman, N.; Bastea, S. Active Learning for Robust,

High-Complexity Reactive Atomistic Simulations. *Journal of Chemical Physics* **2020**, *153*, 134117.

(14) Huy, C.; Pham Lindsey, R. K.; Fried, L. E.; Goldman, N. Calculation of the Detonation State of HN3 with Quantum Accuracy. *Journal of Chemical Physics* **2020**, *153*, 224102.

(15) Lindsey, R. K.; Bastea, S.; Goldman, N.; Fried, L. E. Investigating 3,4-bis(3-nitrofurazan-4-yl)furoxan Detonation with a Rapidly Tuned Density Functional Tight Binding Model. *Journal of Chemical Physics* **2021**, *154*, 164115.

(16) Hofer, L.; Sterling, E.; McCartney, J. Structure of carbon deposited from carbon monoxide on iron, cobalt and nickel. *The Journal of Physical Chemistry* **1955**, *59*, 1153–1155.

(17) Nasibulin, A. G.; Moisala, A.; Brown, D. P.; Kauppinen, E. I. Carbon nanotubes and onions from carbon monoxide using Ni (acac) 2 and Cu (acac) 2 as catalyst precursors. *Carbon* **2003**, *41*, 2711–2724.

(18) Nasibulin, A. G.; Brown, D. P.; Queipo, P.; Gonzalez, D.; Jiang, H.; Kauppinen, E. I. An essential role of CO2 and H2O during single-walled CNT synthesis from carbon monoxide. *Chemical Physics Letters* **2006**, *417*, 179–184.

(19) Nellis, W.; Ree, F.; Van Thiel, M.; Mitchell, A. Shock compression of liquid carbon monoxide and methane to 90 GPa (900 kbar). *The Journal of Chemical Physics* **1981**, *75*, 3055–3063.

(20) Bray, A. Theory of phase-ordering kinetics. *Advances in Physics* **1994**, *43*, 357–459.

(21) Bray, A. Theory of phase-ordering kinetics. *Advances in Physics* **2002**, *51*, 481–587.

(22) Shaw, M.; Johnson, J. Carbon clustering in detonations. *Journal of applied physics* **1987**, *62*, 2080–2085.

(23) Bastea, S. Aggregation kinetics of detonation nanocarbon. *Applied Physics Letters* **2012**, *100*, 214106.

(24) Bastea, S. Nanocarbon condensation in detonation. *Scientific Reports* **2017**, *7*, 42151.

(25) Duane Loh, N.; Sen, S.; Bosman, M.; Tan, S. F.; Zhong, J.; Nijhuis, C. A.; Kral, P.; Matsudaira, P.; Mirsaidov, U. Multistep nucleation of nanocrystals in acqueous solution. *Nature Chemistry* **2017**, *9*, 77–82.

(26) Glotzer, S.; Di Marzio, E.; Muthukumar, M. Reaction-controlled morphology of phase-separating mixtures. *Physical Review Letters* **1995**, *74*, 2034–2037.

(27) Plimpton, S. Fast parallel algorithms for short-range molecular dynamics. *J. Phys. Chem. C* **1995**, *117*, 1–19.

(28) Kohn, W.; Sham, L. J. Self-consistent equations including exchange and correlation effects. *Physical Review* **1965**, *140*, A1133.

(29) https://github.com/rk-lindsey/chimes_calculator.

(30) Leonhardi, T. C.; Militzer, B. Ab initio simulations of liquid carbon monoxide at high pressure. *High Energy Density Physics* **2017**, *22*, 41–45.

(31) Kashchiev, D.; van Rosmalen, G. Review: Nucleation in solutions revisited. *Crystal Research and Technology* **2003**, *38*, 555–574.

(32) Lifshitz, I. M.; Slyozov, V. V. The kinetics of precipitation from supersaturated solid solutions. *Journal of physics and chemistry of solids* **1961**, *19*, 35–50.

(33) Wagner, C. Theorie der alterung von niederschlagen durch umlosen (Ostwald-Reifung). *Zeitschrift Fur Elektrochemie* **1961**, *65*, 581–591.

(34) Voorhees, P. W. The theory of Ostwald ripening. *Journal of Statistical Physics* **1985**, *38*, 231–252.

(35) Siggia, E. Late stages of spinodal decomposition in binary mixtures. *Physical Review A* **1979**, *20*, 595.

(36) Bastea, S.; Lebowitz, J. Spinodal decomposition in binary gases. *Physical Review Letters* **1997**, *78*, 3499–3502.

(37) Hammons, J. A.; Nielsen, M. H.; Bagge-Hansen, M.; Bastea, S.; May, C.; Shaw, W. L.; Martin, A.; Li, Y.; Sinclair, N.; Lauderbach, L. M.; Hodgin, R. L.; Orlikowski, D. A.; Fried, L. E.; Willey, T. M. Submicrosecond aggregation during detonation synthesis of nanodiamond. *The Journal of Physical Chemistry Letters* **2021**, *12*, 5286.

(38) Shimizu, R.; Tanaka, H. A novel coarsening mechanism of droplets in immiscible fluid mixtures. *Nature communications* **2015**, *6*, 7407.

(39) https://github.com/lammps/lammps.

Supporting Information: Chemistry-Mediated Ostwald Ripening in Carbon-Rich C/O Systems at Extreme Conditions

Rebecca K. Lindsey,[*,†] Nir Goldman,[†,‡] Laurence E. Fried,[†] and Sorin Bastea[*,†]

†Physical and Life Sciences Directorate, Lawrence Livermore National Laboratory, Livermore, California 94550, United States

‡Department of Chemical Engineering, University of California, Davis, California 95616, United States

E-mail: lindsey11@llnl.gov; bastea2@llnl.gov

Phone: +1-925-422-0915; +1-925-422-2178

1 Chemical Evolution of the Reactive Fluid

Here we provide an overview of the chemical evolution occurring in the reactive fluid during the appearance and growth of the carbon clusters. As shown in the top plot of Figure 1, the fluid surrounding the clusters is comprised of a variety of small species, though only CO, CO_2, and O are present in notable quantities. The bottom plot of Figure 1 indicates that these small species account for approximately 20% of all carbon in the system, at any given time. The remaining carbon is distributed between clusters, i.e. any set of carbon atoms containing at least 10 members separated by no more than $r_{CC} = 1.9$ Å and "poly" material, i.e. species that are neither nominal clusters nor the small molecules mentioned above. We note that at early times this "poly" material encompasses the polymeric fragments which are precursors to the first carbon clusters, while at late times it contains the remnants of clusters that have been consumed via Ostwald ripening.

2 Oxygen Elimination Kinetics

As noted in the main manuscript, an important part of the cluster evolution is the elimination of interior oxygen; Figure 2 provides an overview of this carbon cluster purification kinetics. The top plot shows a spatially-resolved view of the oxygen content averaged over all the clusters, indicating that initially, oxygen is fairly abundant and largely uniformly distributed. As time progresses, oxygen is found to migrate to cluster exteriors (i.e. larger $r/\langle R_G \rangle$ values). The apparent concomitant oxygen localization at cluster interiors shown in Figure 2 before $\simeq$ 10 ps likely arises from small clusters merging via direct contact (aggregation).

We quantified the elimination kinetics by plotting the amount of oxygen in all clusters larger than the average $r/\langle R_G \rangle$ (i.e. clusters growing via Ostwald ripening), divided by the total number of atoms in these clusters, as a function of time (Figure 2, bottom). The resulting data is well described by a simple exponential relaxation
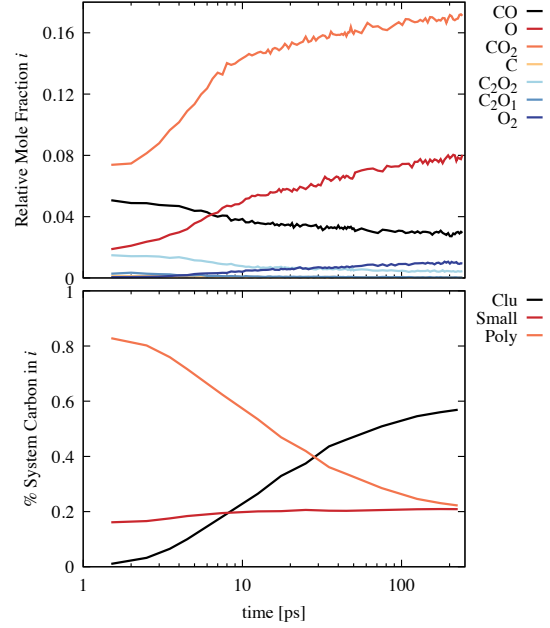

Figure 1: Top: Instantaneous relative mole fractions of small species found in the 1.25×10^6 atom 1:1 C:O system. Bottom: Fraction of carbon in the 1.25×10^6 atom 1:1 C:O system contained in small species, clusters, and "poly" species of intermediate size (i.e. $2 < n_C < 10$).

model ($x = a_0 + a_1 e^{-a_2 t}$, where $a_0 = 0.0078$, $a_1 = 0.18$, and $a_2 = 0.22$); this indicates that the growing clusters likely contain a small fraction of impurity oxygen (i.e. $<1\%$), suggesting non-zero solubility of oxygen in liquid carbon at these conditions.

3 Ostwald Ripening Kinetics: Finite Size Effects

Figure 3, shows that each system with more than $\approx 1.25 \times 10^3$ follows the classical cluster growth trend discussed in the main text (i.e. linear increase in $\langle R_g \rangle^3$ with time). In the three larger systems, we observe two distinct regimes, distinguished by the inflection point at $t \approx 5$ ps separating initial appearance and growth stages, whereas for the smallest cluster-containing system ($\approx 1.25 \times 10^3$ atoms), three regimes emerge. The final flat linear portion of the latter data set is attributed to system size effects, where formation of a single cluster and ensuing growth saturation is observed. Linear fits to the data in-
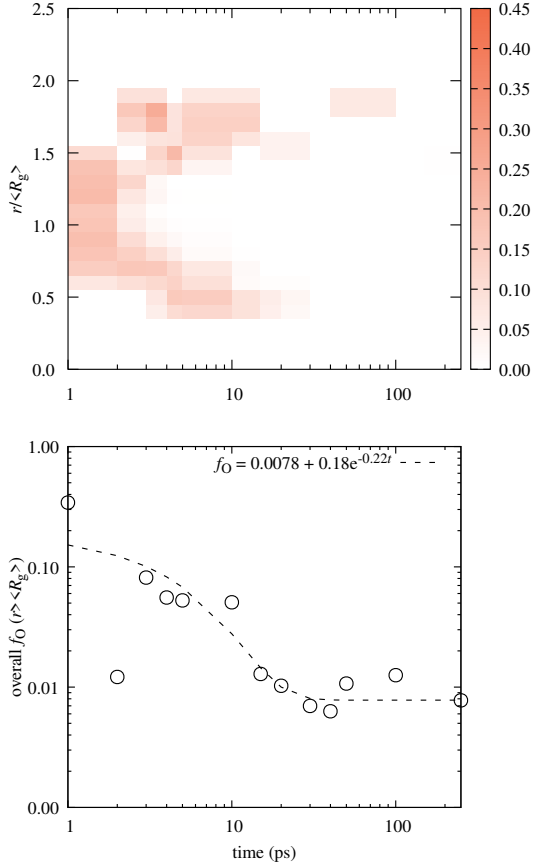
Figure 2: Top: Time resolved location and atomic fraction of oxygen averaged over all clusters. Bottom: Oxygen elimination kinetics for growing clusters (see text).

dicate that growth kinetics are consistent for the larger systems.

We note that the classical growth kinetics observed for the present system enables prediction of $\langle R_g \rangle$ as a function of time, and comparisons with carbon recovery experiments. For example, our recent UF laser-drive shock experiments on CO yielded amorphous carbon clusters of $r = 2.5–15$ nm,[1] suggesting onset quenching times of $\approx 1–2$ ns, in agreement with the experimental time scales.

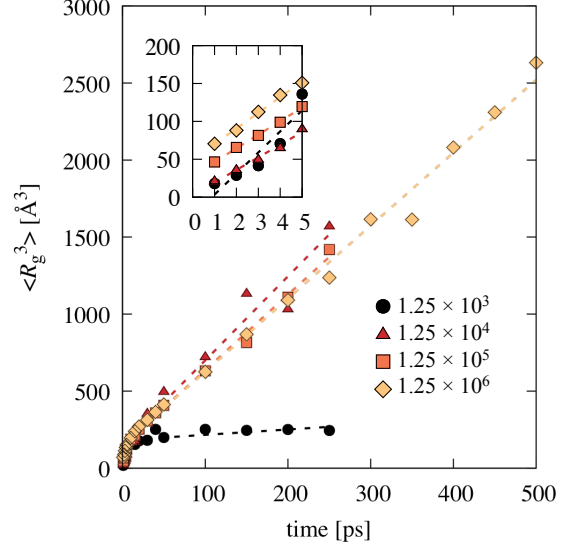Figure 3: Cubed average radius of gyration, $\langle R_g^3 \rangle$, as a function of time for systems containing 1.25×10^3, 1.25×10^4, 1.25×10^5, and 1.25×10^6 atoms. Dashed lines provide linear fits to either $t = 0$ to 5 ps or $t = 5$ to 250 ps and are only intended to serve as a guide to the eye.

4 Cluster Evolution: Finite Size Effects

We provide the average cluster reduced radial density profiles, $\rho(r/R_g)$ and radii of gyration, R_g in Figure 4, for each system with at least 1.25×10^3 atoms. We note that, for clarity, the present analysis considers only carbon atoms within a cluster; since oxygen is located exclusively at the exterior in mature clusters, this assumption has minimal influence on later-time results. In order to generate a given *reduced* radial density profile, a radial density profile was computed for each relevant cluster. A $\rho(r/R_g)$ histogram was then constructed by binning each density profile according to r/R_g. For clarity, the results presented herein correspond to hyperbolic tangent fits to each histogrammed $\rho(r/R_g)$.

For all system sizes, average cluster profiles - Figures 4 - transition from extended, low-density curves at early time to curves indicating an interior density of approximately 3 g/cm^3, with a steep cluster interface. We also find that in all but the 1.25×10^3 system, which forms a single cluster, average cluster radius of gyration, $\langle R_g \rangle$ and minimum radius of gyration, $R_{g,min}$ values
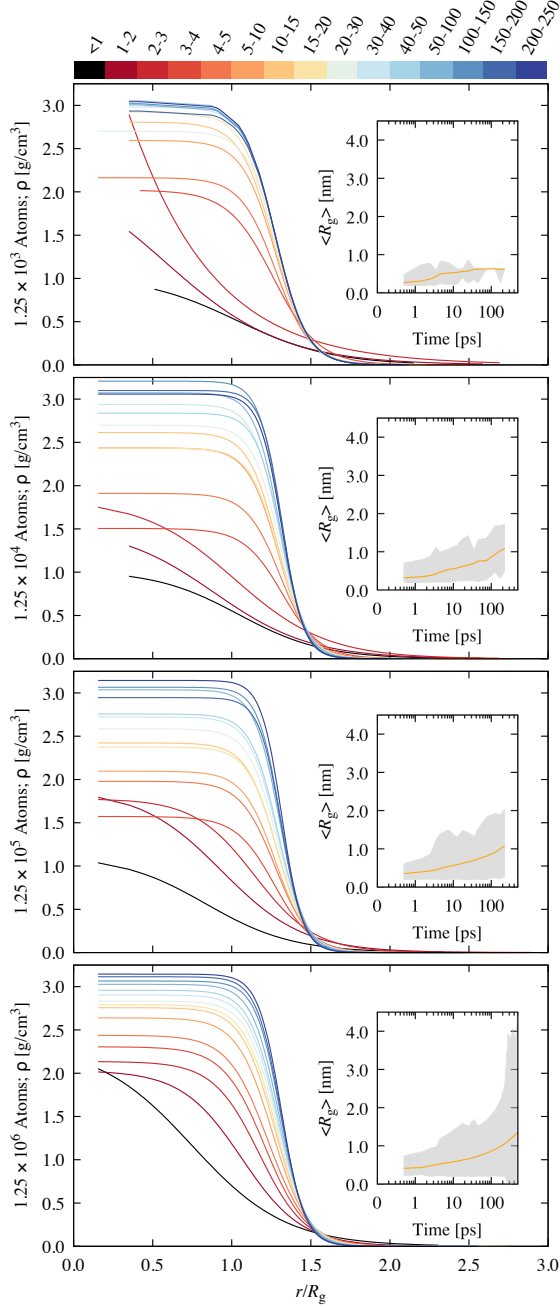
3

Figure 4: Reduced radial density profiles, $\rho(r/R_g)$, and time-resolved average radius of gyration (inset), $\langle R_g \rangle$, for systems containing 1.25×10^3, 1.25×10^4, 1.25×10^5, and 1.25×10^6 atoms. The color bar at the top of the figure provides the time range (in ps) utilized in constructing each density profile. The shaded region in the $\langle R_g \rangle$ inset figures gives the maximum and minimum observed R_g at each time block, while the orange line gives the average value.
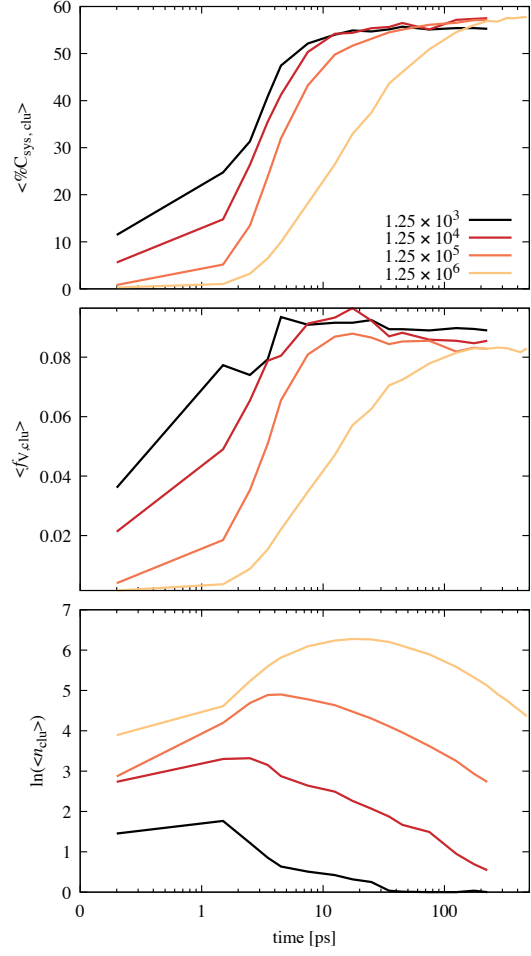
are consistent, with the former value increasing

Figure 5: From top to bottom: average percentage of system carbon participating in cluster formation, $\langle \%C_{sys,clu} \rangle$, average cluster volume fraction, $\langle f_{v,clu} \rangle$, and natural log of the average number of clusters, $\ln\left(\langle n_{clu} \rangle\right)$ for systems containing 1.25×10^3, 1.25×10^4, 1.25×10^5, and 1.25×10^6 atoms.

from approximately 0.4 to 1.0 nm in the first 0.25 ps; $R_{g,max}$ values increase with system size.

5 System Evolution Kinetics: Finite Size Effects

Here we investigate the effects of system size on emergent system kinetics through time-resolved analysis of i. percentage of system carbon participating in cluster formation, $\langle \%C_{sys,clu} \rangle$, ii. total cluster volume fraction, $\langle f_{v,clu} \rangle$, and iii. total number of clusters present in the system, $\langle n_{clu} \rangle$

4

(note that $\langle f_{\mathrm{v,clu}} \rangle$ is computed based on cluster R_{g} values). The results shown in Figure 5 indicate that the evolution trends for each quantity are similar for different system sizes and consistent with Ostwald ripening evolution, and that the number of clusters is most severely affected by finite size effects. The late times values for the percentage of participating carbon and total volume fraction of clusters are in agreement for all systems, and appear to converge as the system size is increased.

6 System Evolution Kinetics: Composition Effects

Atomic composition plays a key role in determining carbon clustering kinetics. For example, energetic materials with different oxygen balance generally exhibit detonation properties differences that can be attributed in part to distinct carbon condensation effects. As noted in the main text, introducing a third (and possibly forth) atom type in our current modeling paradigm should make such simulation studies possible. As a stepping stone to these future efforts we investigate the effects of decreasing the C:O ratio (from 1:1) on the carbon precipitation kinetics. We note that astrophysical studies have suggested that the C:O ratio of both rocky planets and their stars (i.e. under extreme temperature and pressure) is critical for determining overall mineralogy.[2]

The present studies were conducted for systems of $\approx 1.25 \times 10^4$ atoms containing 5, 10, 15, 30, 40, 50, and 75% CO_2, and the balance CO. ($CO_2\%$ and CO as utilized here strictly refer to initial concentrations.) Each of these simulations were conducted at 6500 K and the density determined to yield the same initial pressure as the 0% CO_2 simulations discussed in the main text. Although the system size is relatively small, finite size effects are generally less significant in systems with greater oxygen concentration (less excess carbon). We note that no cluster formation was observed over 0.25 ns for systems with $CO_2 \geq 50\%$.

Figure 6 shows radial composition in the 5:6

C:O system. Cluster chemical evolution proceeds in close similarity with the 1:1 C:O case described in the main text, with early time clusters exhibiting approximately 20% oxygen-containing interiors, and purifying to nearly neat carbon interiors at late time. The 5:6 system also exhibits formation of an oxygen enrichment surface layer, which narrows (relative to the cluster radius) as the cluster matures. The primary difference compared with the 1:1 system is the C/O fractional composition at large r/R_{g}.
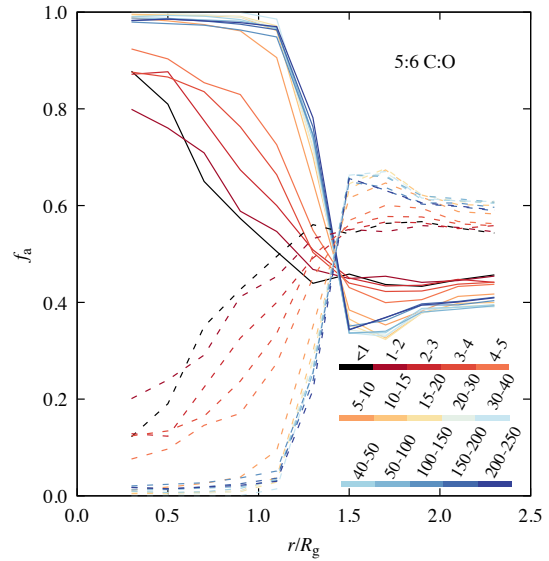

Figure 6: Radial atomic fraction of carbon (solid lines) and oxygen (dashed lines) emanating from cluster centroids, in the 5:6 C:O system. The color bars provide the corresponding time range for each line,.

As shown in Figure 7, maximum values of $\langle \%C_{\mathrm{sys,clu}} \rangle$ (and $\langle f_{\mathrm{v,clu}} \rangle$) are found to decrease as initial CO_2 content is increased from 0 to 40% (C:O ratio decreased from 1:1 to 1:1.4), leveling off at approximately 57% (9%) and 45%(5%), respectively. Systems containing less carbon were found to produce fewer clusters, and to undergo slower kinetics (see Figure 8) during the first ≈ 50 ps, likely due to nucleation effects. At later times, minimal differences in the evolution of average, minimum, and maximum R_{G} are observed, as expected for Ostwald ripening kinetics, with
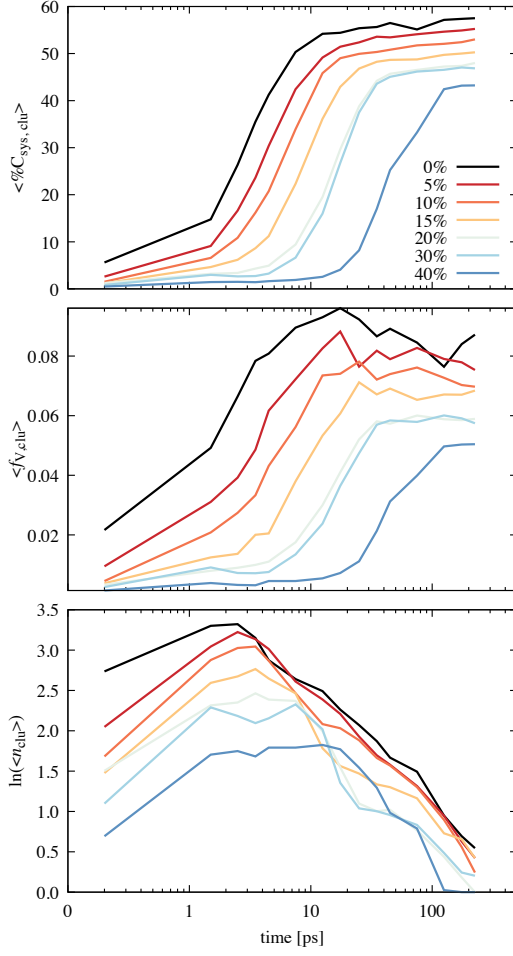
Figure 7: From top to bottom: average percentage of system carbon participating in cluster formation, $\langle \%C_{sys,clu} \rangle$, average cluster volume fraction, $\langle f_{v,clu} \rangle$, and natural log of the average number of clusters, $\ln\left(\langle n_{clu} \rangle\right)$ for systems containing $\approx 1.25 \times 10^4$ atoms, with 0 to 40% of the initial composition CO_2 and the balance, CO .

the exception of the $CO_2 = 40$ % case, where a single cluster is formed.

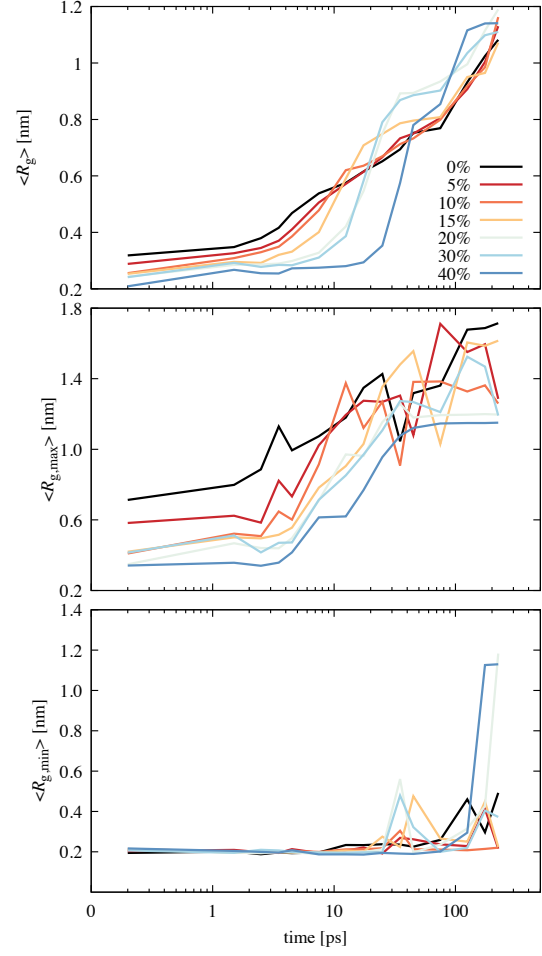Figure 8: From top to bottom: Average, average maximum, and average minimum cluster radius of gyration for systems of varied CO:CO_2 ratio.

References

(1) Armstrong, M.; Lindsey, R.; Goldman, N.; Nielsen, M.; Stavrou, E.; Fried, L.; Zaug, J.; Bastea, S. Ultrafast shock synthesis of nanocarbon from a liquid precursor. *Nature Communications* **2020**, *11*, 353.

(2) Mena, E. D.; Israelian, G.; Hernández, J. G.; Bond, J. C.; Santos, N. C.; Udry, S.; Mayor, M. Chemical clues on the formation of planetary systems: C/O versus Mg/Si for HARPS GTO sample. *The Astrophysical Journal* **2010**, *725*, 2349.